




Multiphase field models for collective cell migration

D. Wenzel ¹ and A. Voigt ^{1,2,3}

¹*Institute of Scientific Computing, Technische Universität Dresden, 01062 Dresden, Germany*

²*Center for Systems Biology Dresden (CSBD), Pfotenhauerstr. 108, 01307 Dresden, Germany*

³*Cluster of Excellence–Physics of Life, TU Dresden, 01062 Dresden, Germany*

 (Received 22 June 2021; revised 18 September 2021; accepted 5 November 2021; published 24 November 2021)

Confluent cell monolayers and epithelia tissues show remarkable patterns and correlations in structural arrangements and actively driven collective flows. We simulate these properties using multiphase field models. The models are based on cell deformations and cell-cell interactions and we investigate the influence of microscopic details to incorporate active forces on emerging phenomena. We compare four different approaches, one in which the activity is determined by a random orientation, one where the activity is related to the deformation of the cells, and two models with subcellular details to resolve the mechanochemical interactions underlying cell migration. The models are compared with respect to generic features, such as coordination number distribution, cell shape variability, emerging nematic properties, as well as vorticity correlations and flow patterns in large confluent monolayers and confinements. All results are compared with experimental data for a large variety of cell cultures. The appearing qualitative differences of the models show the importance of microscopic details and provide a route towards predictive simulations of patterns and correlations in cell colonies.

DOI: [10.1103/PhysRevE.104.054410](https://doi.org/10.1103/PhysRevE.104.054410)

I. INTRODUCTION

The ability of cells to coordinate their motion is essential for several *in vivo* processes, such as morphogenesis, regeneration, and cancer invasion [1–3]. To identify the principles that govern collective cell migration in such systems has seen a growing interest in recent years. Experimental investigations on cell monolayers and epithelial tissue of model systems have shown remarkable patterns and correlations in cell migration. These include an unjamming transition between a glassy phase and a fluid phase [4,5], the spontaneous formation of vortices and topological defects [6], as well as the emergence of active turbulent flows [7]. The emerging phenomena appear to be rather generic. A fundamental challenge is to understand how this macroscopic behavior is linked to the properties of individual cells and physical cell-cell interactions, which is the target of a large variety of modeling approaches. These approaches differ by the level of coarse-graining and range from subcellular lattice models [8] and multiphase field models [9–14], to vertex and Voronoi models [15–19], particle models [20–24], and continuum models on a multicellular scale [25–27]. We refer to [28–30] for recent reviews.

We here concentrate on multiphase field models, which allow for cell deformations and detailed cell-cell interactions, as well as subcellular details to resolve the mechanochemical interactions underlying cell migration. Together with efficient numerics and appropriate computing power these models are well suited to model confluent cell structures and have seen various recent contributions [9–14]. They all follow the same methodology but differ in detail. Until now these models have been used to address specific problems but have never been compared with each other.

The goal of this paper is a systematic comparison of these approaches and their linkage with statistical observables of experiments to provide a route towards predictive simulations of patterns and correlations in cell colonies. After introducing the multiphase field models, discussing microscopic differences, and briefly describing the numerical approach enabling large-scale simulations, we address coordination number distribution, analyze statistics on shape variability of the cells and the ratio of multicellular rosettes, velocity distributions of emerging topological defects, their stress fields, as well as defect density and creation rates. We further study vorticity correlations in large confluent monolayers and flow patterns in confinements. All results are compared with experimental data for a large variety of cell cultures. The appearing qualitative differences of the models show the importance of microscopic details. The systematic comparison will hopefully help to select the appropriate approach in future studies and provide a route towards predictive simulations of patterns and correlations in cell colonies.

II. MODELING

We consider two-dimensional phase field variables ϕ_i , one for each cell. Values of $\phi_i = 1$ and $\phi_i = -1$ denote the interior and the exterior of a cell, respectively. The cell boundary is defined implicitly by the $\phi_i = 0$ level set. The dynamics for each ϕ_i is considered as

$$\partial_t \phi_i + v_0(\mathbf{v}_i \cdot \nabla \phi_i) = \Delta \frac{\delta \mathcal{F}}{\delta \phi_i}, \quad i = 1, \dots, N, \quad (1)$$

where N denotes the number of cells, \mathcal{F} is a free energy, and \mathbf{v}_i a vector field used to incorporate active components, with a self-propulsion strength v_0 . We here consider conserved

dynamics, which ensures constant volume/area of each cell. The proposed models in [9,11,12,14] consider nonconserved dynamics and enforce the volume/area constraint weakly by an additional penalty energy. The free energy $\mathcal{F} = \mathcal{F}_{\text{CH}} + \mathcal{F}_{\text{INT}} + \dots$ contains passive contributions, where

$$\mathcal{F}_{\text{CH}} = \sum_{i=1}^N \frac{1}{\text{Ca}} \int_{\Omega} \frac{\epsilon}{2} \|\nabla \phi_i\|^2 + \frac{1}{\epsilon} W(\phi_i) d\mathbf{x}, \quad (2)$$

$$\mathcal{F}_{\text{INT}} = \sum_{i=1}^N \frac{1}{\text{In}} \int_{\Omega} B(\phi_i) \sum_{j \neq i} w(d_j) d\mathbf{x}, \quad (3)$$

with nondimensional capillary and interaction number, Ca and In, respectively. The first is a Cahn-Hilliard energy, with $W(\phi_i) = \frac{1}{4}(\phi_i^2 - 1)^2$ a double-well potential and ϵ a small parameter determining the width of the diffuse interface. This energy stabilizes the cell interface. For simplicity we here neglect other properties of the cell boundary, e.g., bending forces. In [31] they are shown to be negligible in the context of cell migration. The second is an interaction energy with $B(\phi_i) = \frac{3}{\epsilon\sqrt{2}} W(\phi_i)$ an approximation of the delta function of the cell boundary and a cell-cell interaction potential

$$w(d_j) = \exp\left(-\frac{d_j^2}{\epsilon^2}\right), \quad \text{with } d_j = -\frac{\epsilon}{\sqrt{2}} \ln\left(\frac{1 + \phi_j}{1 - \phi_j}\right) \quad (4)$$

approximating a short-range repulsion potential, with signed distance function d_j computed from the equilibrium tanh profile of the phase field ϕ_j (see [32,33]). Most previous multiphase field models consider the interaction only effectively using terms proportional to $\phi_i^2 \phi_j^2$ for cell-cell repulsion and $\|\nabla \phi_i\|^2 \|\nabla \phi_j\|^2$ for cell-cell attraction. The approach in Eq. (4) offers the possibility to also consider more realistic potentials. Most significantly the proposed models [9–14] differ in the self-propulsion term, the definition of \mathbf{v}_i in Eq. (1).

In [14] the propulsion speed is the same for each cell, but the direction of motion, determined by the angle θ_i , is controlled by rotational noise $d\theta_i(t) = \sqrt{2D_r} dW_i(t)$, with diffusivity D_r and a Wiener process W_i . With $\mathbf{v}_i^{\text{ran}} = (\cos \theta_i, \sin \theta_i)$ the governing equations can be viewed as a generalization of a model for active Brownian particles [20,34,35] to one for a system of deformable cells. Subcellular details are not considered.

In [12] the propulsion of each cell is related to its deformation. For each phase field variable ϕ_i a Q tensor (symmetric and trace-free) is defined by

$$\mathbf{S}_i = \int \begin{bmatrix} \frac{1}{2}[(\partial_y \phi_i)^2 - (\partial_x \phi_i)^2] & -(\partial_x \phi_i)(\partial_y \phi_i) \\ -(\partial_x \phi_i)(\partial_y \phi_i) & \frac{1}{2}[(\partial_x \phi_i)^2 - (\partial_y \phi_i)^2] \end{bmatrix} d\mathbf{x}$$

from which a continuous Q -tensor field $\mathbf{S} = \sum_{i=1}^N \mathbf{S}_i \tilde{\phi}_i$ can be constructed by interpolation, with $\tilde{\phi}_i$ a rescaled phase field variable with values in $[0,1]$. The active contribution is defined as $\mathbf{v}_i^{\text{elo}} = \int \tilde{\phi}_i \nabla \cdot \mathbf{S} d\mathbf{x}$. While the strength and the direction is constant within a cell, both differ between cells. Also in this approach, subcellular details are not considered. However, the coupling with neighboring cells becomes stronger as they have an influence on the cell deformation.

Subcellular details, modeled as an active polar gel, have been considered in [31,36–38]. In these approaches for a

single active droplet cell movement results from spontaneous symmetry breaking in the polarization field of the subcellular, e.g., actin, filaments. This route to cell motility is used in [32,39] for collective cell migration and applied to simulate confluent cell structures in [13,40]. The free energy \mathcal{F} has to be extended by a Frank-Oseen type energy

$$\mathcal{F}_{\mathbf{P}} = \sum_{i=1}^N \frac{1}{\text{Pa}} \int_{\Omega} \frac{1}{2} \|\nabla \mathbf{P}_i\|^2 + \frac{c^p}{4} \|\mathbf{P}_i\|^2 (-2\phi_i + \|\mathbf{P}_i\|^2) + \beta \mathbf{P}_i \cdot \nabla \phi_i d\mathbf{x} \quad (5)$$

with polarization field \mathbf{P}_i for each cell and nondimensional elastic parameter Pa. The second term ensures the unity constraint weakly in the interior, $\phi_i = 1$, and forces $\mathbf{P}_i = 0$ in the exterior, $\phi_i = -1$, with $c^p > 0$, and the third term sets an anchoring condition at the cell boundary, $\nabla \phi_i \neq 0$, with $\beta > 0$. The dynamics for each \mathbf{P}_i is considered as

$$\partial_t \mathbf{P}_i = -\frac{\delta \mathcal{F}}{\delta \mathbf{P}_i}, \quad i = 1, \dots, N. \quad (6)$$

In contrast to previous models [13,32,39] self-advection in the evolution equation for \mathbf{P}_i is omitted, to allow for better comparability with the other models. The coupling with Eq. (1) follows by defining $\mathbf{v}_i^{\text{pol}} = \mathbf{P}_i$. While the local strength remains constant, the active force is no longer equally distributed over the cell as the direction results from the subcellular polarization field, which is strongly influenced by the geometry of the cell. On the single cell level, cell movement results in the considered setting from contractile stress (see [31,36] for details and possible modifications to generate motion by extensile stress).

As an alternative modeling approach with subcellular details we consider instead a polar structure nematic ordering within each cell. A nematodynamic approach has been considered in [41,42] to model movement of a single active nematic droplet. We here simplify this approach and extend it to multiple cells. The free energy \mathcal{F} is extended by a Landau-de Gennes type energy

$$\mathcal{F}_{\mathbf{Q}} = \sum_{i=1}^N \frac{1}{\text{Ne}} \int_{\Omega} \frac{1}{2} \|\nabla \mathbf{Q}_i\|^2 + \text{tr} \mathbf{Q}_i^2 \left(-\frac{c^n}{2} \phi + \frac{c^n}{4} \text{tr} \mathbf{Q}_i^2 \right) + \gamma \nabla \phi_i \mathbf{Q}_i \nabla \phi_i d\mathbf{x} \quad (7)$$

with Q -tensor field \mathbf{Q}_i for each cell and nondimensional elastic parameter Ne. The second term enforces $\mathbf{Q}_i = 0$ in the exterior of the cell, with $c^n > 0$ and the third term again sets an anchoring condition at the cell boundary, with $\gamma > 0$. The dynamics for each \mathbf{Q}_i reads

$$\partial_t \mathbf{Q}_i = -\frac{\delta \mathcal{F}}{\delta \mathbf{Q}_i}, \quad i = 1, \dots, N, \quad (8)$$

and $\mathbf{v}_i^{\text{nem}} = \nabla \cdot \mathbf{Q}_i$. In this approach the strength and direction of the active force for each cell results from subcellular structures and varies within the cell and between cells. The influence of the cell shape on the resulting movement is much stronger and a clear distinction between contractile and extensile behavior on a single cell level is not generally possible.

The differences of the models are visualized in Fig. 1 for one representative cell. $\mathbf{v}_i^{\text{ran}}$ is constant within the interior of

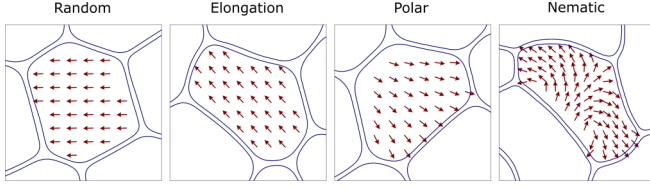


FIG. 1. Visualization of representative \mathbf{v}_i within one cell in confluent cell structure. From left to right: $\mathbf{v}_i^{\text{ran}}$, $\mathbf{v}_i^{\text{elo}}$, $\mathbf{v}_i^{\text{pol}}$, and $\mathbf{v}_i^{\text{nem}}$. The length of the arrows is rescaled to be comparable; the blue lines indicate the $\phi_i = 0$ level sets of the considered cell and its neighbors.

the cell. While this is also true for $\mathbf{v}_i^{\text{elo}}$, here the direction is aligned with the long axis of the cell. $\mathbf{v}_i^{\text{pol}}$ shows the typical splay instability resulting from contractile stress [31,36] with a preferred mean orientation but otherwise constant local strength. $\mathbf{v}_i^{\text{nem}}$ shows a more complex behavior. The underlying instability in this model results in a rearrangement of the topological defects in the Q -tensor field \mathbf{Q}_i , which strongly depends on the geometry of the cell and leads to no preferred mean orientation of $\mathbf{v}_i^{\text{nem}}$. To explore the influence of these differences on macroscopic observables is the target of this paper.

III. NUMERICS AND PARAMETER SETTING

We employ a parallel and adaptive finite element method to solve the coupled system of partial differential equations for ϕ_i and \mathbf{P}_i or \mathbf{Q}_i , for $i = 1, \dots, N$, numerically. The algorithm is implemented in AMDiS [43,44] and the algorithmic concepts to achieve parallel scaling with the number of cells N are described in [45]. Briefly, they consider one core for the evolution of each cell and parallel concepts from particle methods to reduce the communication overhead due to cell-cell interaction.

We consider a constant number of equally sized cells (no cell divisions and apoptosis). First, $N = 100$ cells in a rectangular domain, $\Omega = [0, 100] \times [0, 100]$, with periodic boundary conditions are considered. This approximates a large confluent monolayer with no need for confinement. Second, confinements are realized in the same computational domain Ω by an implicit description using a phase field variable $\phi_\delta(\mathbf{x}) = \tanh[(\|\mathbf{x} - \mathbf{c}\| - 50)/(\sqrt{2}\epsilon)]$, where $\mathbf{c} = (50, 50)^T$ and the choice of the vector norm determines the confinement shape. In particular, we use $\|\cdot\|_2$ for a circular confinement with diameter 100. The repulsive force of the confinement is introduced using an interaction potential as in Eq. (4) and an additional energy contribution

$$\mathcal{F}_{C_0} = \sum_{i=1}^N \frac{1}{C_0} \int_{\Omega} B(\phi_i) w(d_\delta) d\mathbf{x},$$

following the approach of Eq. (3). Within the circular confinement there are $N = 106$ cells, resulting from regular initial arrangements. In order to avoid minimal energy configurations as initial conditions, we start with rectangular cells but avoid higher-order vertices. Various test simulations confirm that the presented results are independent of these initial configurations. Considering the zero-level set of ϕ_i as cell boundary the resulting packing fraction is around 90%. The

TABLE I. Chosen values for v_0 classified as low, medium, and high activity.

	Random	Elongation	Polar	Nematic
Low	1.2	1.0	1.2	21.0
Medium	2.4	2.0	2.4	24.0
High	3.6	3.0	3.6	30.0

model parameters are chosen as $\epsilon = 0.15$, $\text{In} = 0.025$, $\text{Pa} = \text{Ne} = 1$, $\text{Co} = 0.004$, and $c^p = c^n = 1$. We further consider $D_r = 0.1$, $\beta = 0.01$, and $\gamma = 0.1$. This allows one to only vary Ca and v_0 . Other numerical parameters, such as grid resolution and time step, are considered as large as possible to ensure stable behavior and resolution of the essential physics. The grid spacing within the diffuse interface is $h \approx 0.2\epsilon$, in the interior of each cell $h \leq \epsilon$, and in the exterior $h \leq 10\epsilon$ with increasing values for regions far away from the interior. The time step is chosen as $\tau = 0.1$.

IV. COORDINATION NUMBER DISTRIBUTION AND SHAPE VARIABILITY

Coordination number distribution has been extensively studied in vertex and Voronoi models (see, e.g., [19]), and identified to depend on the strength of activity and cell deformability. While the deformability is typically described in these models using a shape index, we here follow [14] and directly consider the surface tension, respectively the capillary number Ca .

The coordination number q , i.e., the number of neighboring cells, is measured after an initialization phase, making sure the evaluated quantities are independent on time. Figure 2 (first row) shows the averaged distribution over all cells and all time steps for fixed Ca and various v_0 for the four models. We consider three representative levels of activity, termed low, medium, and high. The precise choice of v_0 depends on the mechanism of activity but is kept constant throughout the following chapters and can be found in Table I. For all models the mean value of the coordination number probability is close to 6 and only slightly decreases with increasing activity. The coordination number is an easily accessible structural property, which can be used as a rough measure to identify solid-to-liquid transitions [14]. Considering the coordination number q to deviate from the hexagonal ordering, which can be expressed by the statistic variance $\mu = \sum_q (q - 6)^2 P(q) > \theta_{P(q)}$, with $P(q)$ the discrete probability distribution obtained from counting the presence of each value q and $\theta_{P(q)} = 0.001$, we can identify the solid and liquid phase. Figure 2 (second row) shows the phase diagram for the four models. Blue are regions where the observable indicates solidlike behavior and red are regions where it indicates liquidlike behavior.

Although the qualitative behavior of the phase diagram is quite similar for all four models and the previous studies using vertex and Voronoi models [19], the actual quantitative results in terms of the parameter range for v_0 differ strongly. Both the random and the polar model are driven by a normalized vector field with a clearly preferred direction which results in a quantitatively similar behavior. For the elongation-based and

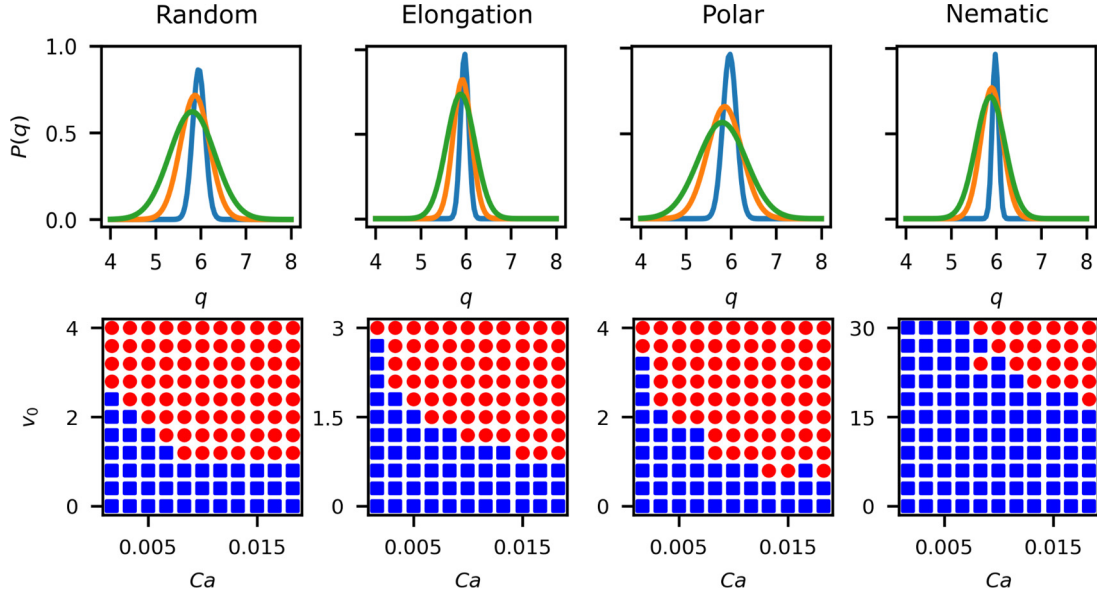


FIG. 2. First row: Coordination number probability for $Ca = 0.0148$ with low (blue), medium (orange), and high (green) values of v_0 . For actual values, see Table I. Second row: Phase diagram indicating the transition between solid (blue) and liquid (red) states as a function of the deformability parameter (capillary number) Ca and the activity (self-propulsion strength) v_0 .

the nematic model the driving force is computed as divergence of a tensor field and thus not normalized, indicating why they have a parameter range which is different from the other two models.

The snapshots in Fig. 3 show typical cell shapes for the four models in the liquid and solid phase, respectively. The cell shapes are isotropic on average in the solid phase and anisotropic in the liquid phase, leading to differences in the number of neighbors. Also the cell tracks significantly differ; they show dynamical arrest due to caging in the solid phase and diffusion in the liquid phase. These tracks are obtained by considering the center of mass of each cell in each time step. While the solid phase is more or less identical in all four models, the liquid phase differs significantly. We will quantify these differences below.

Following [5], it should also be possible to identify common generic features over a wide range of the phase diagrams. Considering the shape variability of the cells, which is ex-

pressed by the aspect ratio AR of the long and the short cell axis, the largest and the smallest eigenvalue of \mathbf{S}_i , and rescaling $x = \frac{AR}{\langle AR \rangle}$, with $\langle \cdot \rangle$ the average value, leads to an empirically proposed universal k -gamma distribution [5] with probability distribution function $\text{PDF}(x, k) = \frac{k^k}{\Gamma(k)} x^{k-1} e^{-kx}$ with Legendre gamma function $\Gamma(k)$. This distribution is fully described by the parameter k and has a mean of unity. Across diverse epithelia systems, including Madin-Darby canine kidney (MDCK) cells, human bronchial epithelia cells (HBECS), and the *Drosophila* embryo during ventral furrow formation, [5] shows that this equation pertains to k in a narrow range between 2 and 3, which indicates universality. This result provides the first quantitative comparison for the different phase field models. Figure 4 shows the distribution for all four models together with maximum-likelihood-estimation fits for $\text{PDF}(x, k)$ for three different parameters v_0 and $Ca = 0.018$. The corresponding k values for each v_0 are shown in Table II.

Indeed, in accordance with the experimental results in [5], the data can be described by a k -gamma distribution and k does not vary strongly within each model for the considered parameters. However, the k values differ between the four models. While both the elongation-based and the polar model have values within the experimentally predicted universal

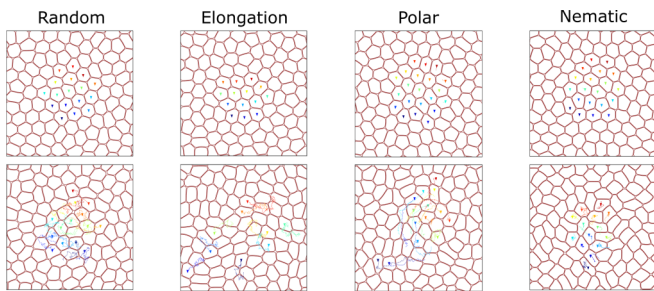


FIG. 3. Snapshots of tissue morphology for liquid phase (first row) and solid phase (second row), for the four models, random, elongation, polar, and nematic (from left to right). Shown are the zero-level sets of ϕ_i together with cell trajectories for some time span of the cells in the center, indicating diffusion in the liquid phase and dynamical arrest due to caging in the solid phase.

TABLE II. k -gamma parameter fit for different models. Low, medium, and high correspond to the values used in Fig. 4. The k values are obtained with maximum-likelihood-estimation fits for $\text{PDF}(x, k)$ for one simulation run over the whole time.

v_0	Random	Elongation	Polar	Nematic
Low	3.18	2.68	2.82	3.23
Medium	3.12	2.60	2.87	4.20
High	3.04	2.49	2.85	4.21

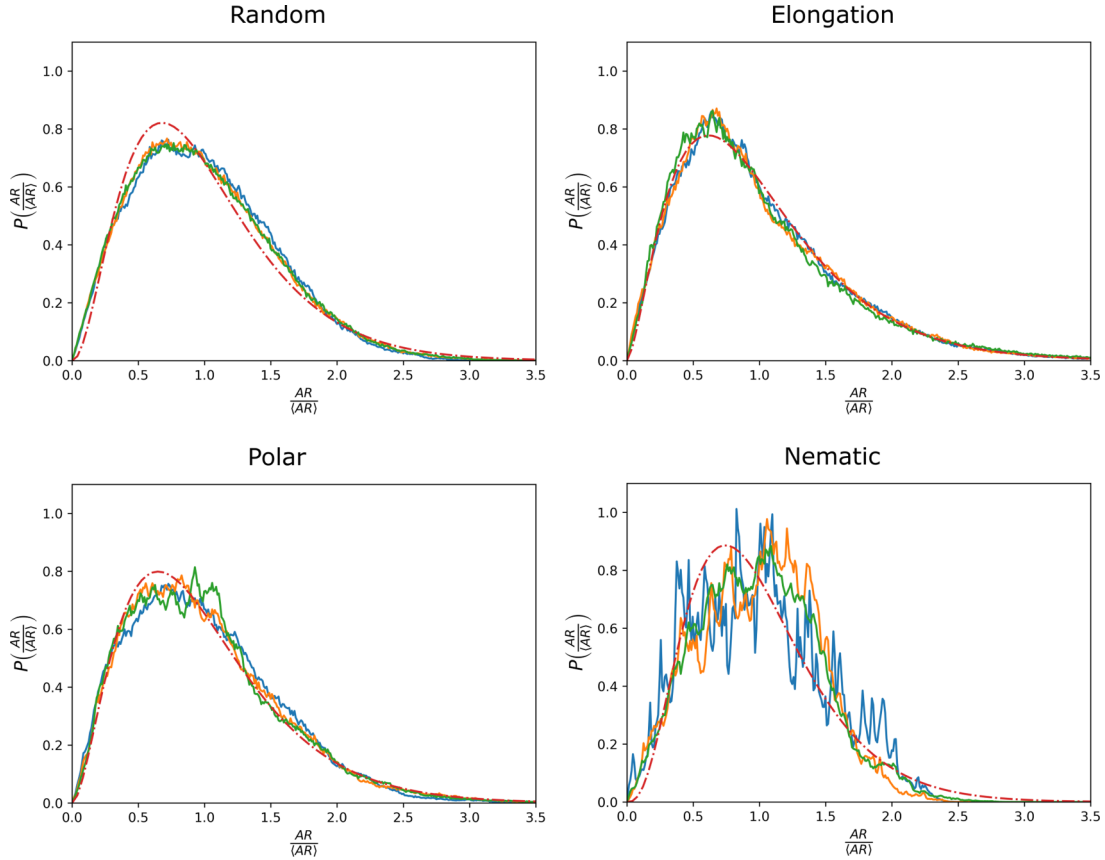


FIG. 4. Shape variability for the four models using the rescaled parameter $x = \frac{AR}{\langle AR \rangle}$ for different points of the phase diagrams in Fig. 2 with low (blue), medium (orange), and high (green) activity. Fitted values for the PDF (red) are computed using data for all three values v_0 resulting in $k^{\text{ran}} = 3.11$, $k^{\text{elo}} = 2.59$, $k^{\text{pol}} = 2.84$, and $k^{\text{nem}} = 3.88$.

range between 2 and 3, both the random and the nematic model are slightly above with the latter one leading to the largest values. These larger values for k in the nematic model become evident from the construction of the model, where active forces enhance elongation which is also apparent in Fig. 1. This also explains why k is growing for larger values of v_0 only in the nematic model while it stays approximately constant in all others. The larger fluctuations in the polar and especially the nematic model can be explained by the stronger coupling between shape changes and active forces.

These differences in the shape variability of the cells provide a first indication on the dependency of macroscopic observables on the microscopic details considered in each model.

V. LIQUID PHASE

We now only concentrate on the liquid phase and compare the four models with other statistical observables of experiments. We consider vorticity correlation functions and statistical data on topological measures, such as number of neighboring cells and distributions of topological defects. In order to be comparable we parametrize all models to fulfill one common topological measure. While the deformability parameter, the capillary number, can be chosen as $Ca = 0.018$ in all models, the activity parameter v_0 differs to model the same physical state in the phase diagram. We consider

the variance in the coordination number $\mu = 0.4$ as a reference value. This value corresponds to a value measured in *Drosophila* embryos [46] at an early stage of development (up to stage 7 before intercallation). Using $v_0^{\text{ran}} = 1.3$, $v_0^{\text{elo}} = 0.6$, $v_0^{\text{pol}} = 1.3$, and $v_0^{\text{nem}} = 19.0$, we obtain $\mu = 0.41$, 0.40 , 0.44 , and 0.45 , respectively. The resulting configurations with these parameters are considered as comparable physical states.

A. Rosette formation

Multicellular rosettes or higher-order vertices, where four or more cells meet, have been found in many tissues [47,48]. The importance of cellular rosettes has been widely recognized and they have been proposed as an efficient mechanism for tissue remodeling. In [49] the influence of rosettes on the mechanics of a confluent tissue is studied using a generalized vertex model. While in these models the formation of rosettes requires a collapse of cell edges, T1 junctions and rosettes form naturally within our multiphase field models [13]. The considered parameters lead to the formation of rosettes. The rosette ratio, the fraction of all vertices that connect more than three cells, is shown in Table III.

The rosette ratio has been measured in various developmental processes. Experimental data for the rosette ratio for the early stage of development (up to stage 7 before intercallation) in *Drosophila* embryos [46] show values between 5%

TABLE III. Average rosette ratio for different models, considered for one simulation over a time interval after initialization for comparable physical states.

	Random	Elongation	Polar	Nematic
Rosette ratio	4.8%	2.6%	5.5%	1.3%

and 6%. The considered parameters can at least phenomenologically be linked to this situation. The measured values are reproduced by the polar model. The random model leads to a ratio which is only slightly below. The other two models lead to significantly lower values. Even if only one physical state is considered, which allows for a calibrated comparison with experimental data, the results strongly differ between the four models. These differences on the rosette ratio indicate a further dependency on the mechanism of propulsion.

B. Nematic order and topological defects

Many cellular systems in its liquid phase display properties of active liquid crystals, such as local nematic alignment and the appearance of topological defects. For MDCK cells it has been shown that these defects can control death and extrusion in cell monolayers [6]. This relation has been used to model collective cell migration on a multicellular scale (see [27]). In [12] the formation of nematic order is addressed using a multiphase field model. We follow this procedure and compare the emergence of global nematic order and the proliferation of topological defects in the orientation field in all four models. We thereby determine nematic order from cell deformations and compute the local Q tensor \mathbf{S}_i for each phase field ϕ_i . The eigenvalues and eigenvectors of \mathbf{S}_i measure the strength and orientation of the main deformation axis of cell i . Interpolating \mathbf{S}_i , as described for the elongation-based model above, defines a global Q tensor \mathbf{S} . Different methods exist to identify topological defects in \mathbf{S} ; they have been compared in [40]. We here consider a physics-based approach, which addresses degenerated points of \mathbf{S} to identify the location of defects and the sign of $\delta = \partial_x S_{11} \partial_y S_{12} - \partial_y S_{11} \partial_x S_{12}$ to distinguish between $+\frac{1}{2}$ and $-\frac{1}{2}$ defects. Figure 5 illustrates the process for one snapshot.

Localization and identification of defects is done in each time step. In order to connect the defects from frame to frame we consider a particle tracking algorithm [50], available in ImageJ/Fiji [51] and shown to reliably consider different defect types and defect appearance and disappearance [40]. This allows one to statistically examine the velocity distribution of topological defects in all four models (see Fig. 6).

While these distributions strongly differ between the four models, in all models the velocity distribution of $+\frac{1}{2}$ and $-\frac{1}{2}$ defects is similar. This qualitative difference with coarse-grained active nematodynamics and experimental data, e.g., for active microtubule networks, which indicate a difference in the velocity distribution between the different types of defects (see [52,53]), has already been found in [40]. Detailed data on the velocity distribution of $+\frac{1}{2}$ and $-\frac{1}{2}$ defects for epithelia cell cultures are not separately available. However, for HBECs, [7] indicates no apparent quantitative differences

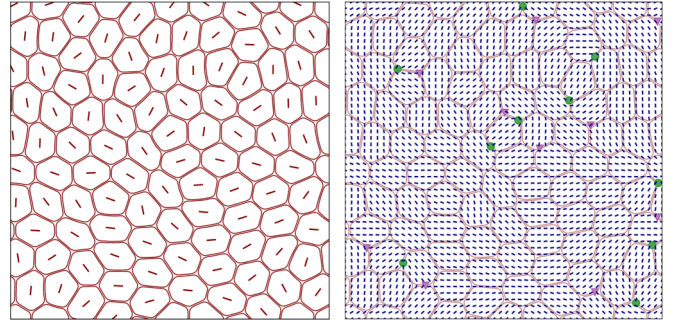


FIG. 5. Left: Tissue morphology represented by $\phi_i = 0$ level lines, together with the normalized largest eigenvector of \mathbf{S}_i corresponding to the orientation of the long cell axis in the center of mass of each cell (red lines). Right: Global nematic field \mathbf{S} obtained by interpolation of \mathbf{S}_i , represented by director field (blue lines) and $+\frac{1}{2}$ (green) and $-\frac{1}{2}$ (purple) defects. The $\phi_i = 0$ level lines are shown to indicate the position of defects in relation to the morphology.

between both types of defects in terms of their trajectories on long timescales, which might support the simulation results. However, differences between $+\frac{1}{2}$ and $-\frac{1}{2}$ defects become evident if the direction of the defect velocity is correlated with the local properties of the defect. Figure 7 shows the distribution of directions with respect to symmetry properties of $+\frac{1}{2}$ and $-\frac{1}{2}$ defects.

While the velocity of $-\frac{1}{2}$ defects do not show any preferred orientation for all models, which supports the passive (diffusive) role of these defects, the velocity of $+\frac{1}{2}$ defects is strongly correlated with the head or the tail of the defect. Only the random model does not show this property. All other models support the active role of $+\frac{1}{2}$ defects in active nematic systems [27]. The elongation model shows a strong correlation of the direction of movement with the head of the defect, indicating extensile behavior. The polar and nematic models show a stronger correlation with the tail of the defect, indicating contractile behavior. For a detailed discussion of these relations in active nematics we refer to [54].

To further elaborate on the hypothesis that microscopic details on the single cell level determine the mechanical properties of the system, we compute the strain rate tensor in the vicinity of $+\frac{1}{2}$ defects. The essential quantity is the velocity \mathbf{v} obtained by linear interpolation of the cell velocities $\mathbf{v}_i^{\text{cell}}$, which are computed from the movement of the center of mass of the cells. The strain rate tensor $\mathbf{E} = \frac{1}{2}[\nabla\mathbf{v} + (\nabla\mathbf{v})^T]$ is defined in the vicinity of the $+\frac{1}{2}$ defects and averaged after appropriate reorientation over all defects. Figure 8 shows the averaged fields for all models.

With the exception of the random model, which does not show any significant pattern, the other models support our hypothesis. The elongation model leads to patterns characteristic for extensile systems, while the polar and nematic models show patterns characteristic for contractile systems. The strain rate along the tail-to-head direction (yy strain) shows negative (positive) values at the head indicating the presence of compression (extensional deformation). The presence of both types is known from experiments, e.g., epithelial [6,7] or neural progenitor [55] monolayers behave as an extensile

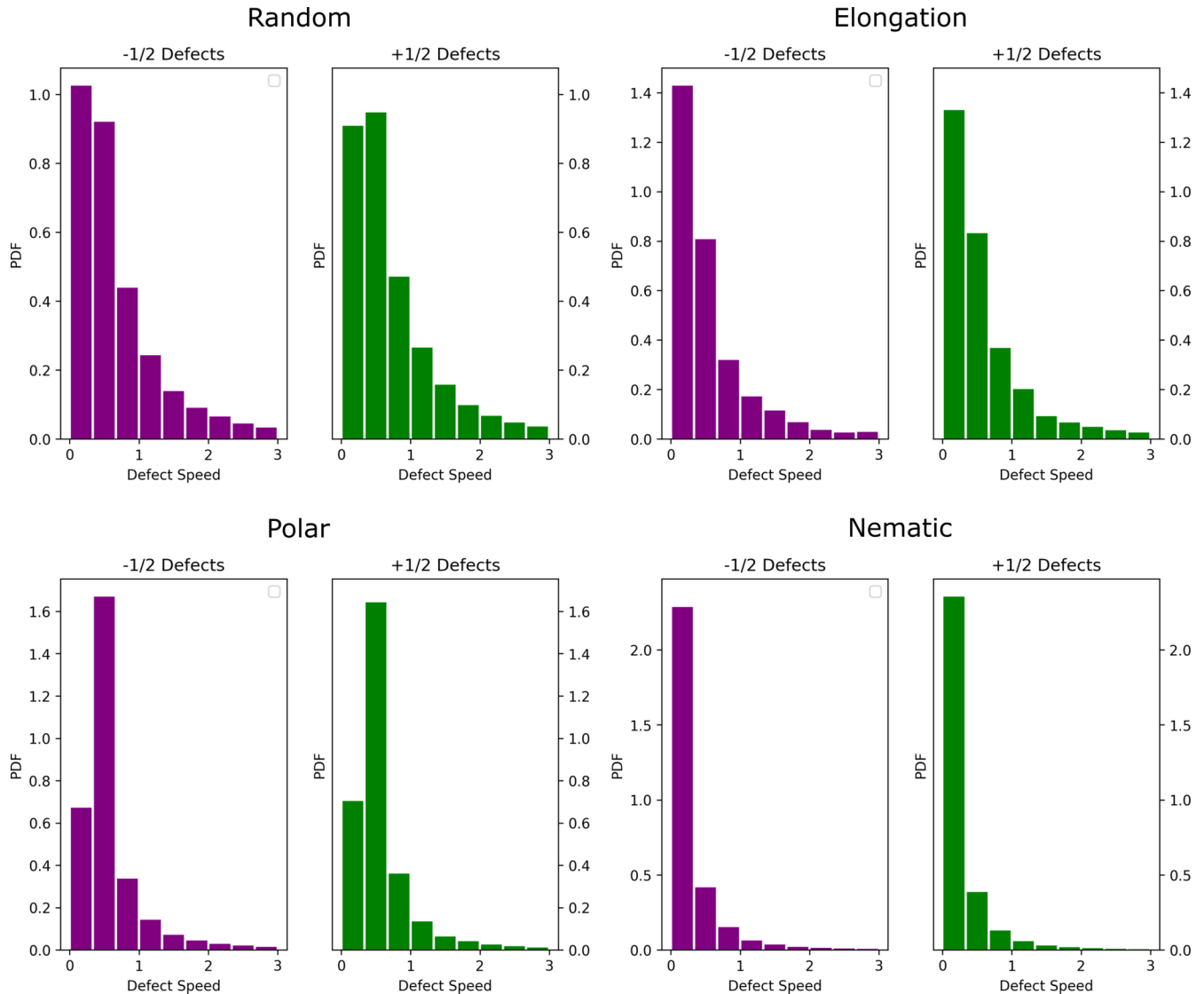


FIG. 6. Velocity distribution of topological defects ($+\frac{1}{2}$ and $-\frac{1}{2}$) for all four models: random, elongation, polar, and nematic, from top left to bottom right.

system, while monolayers of fibroblasts [56] behave as a contractile system. The extensile behavior of the elongation

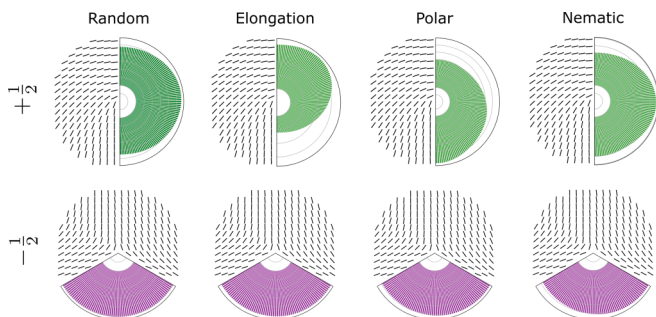


FIG. 7. Distribution of direction of motion with respect to symmetry properties of $+\frac{1}{2}$ (top) and $-\frac{1}{2}$ (bottom) defects for all four models. A schematic description of the defects defines the considered symmetry.

model has already been found in [12]. The model is constructed to elongate the cell further along its long axis (see definition of \mathbf{v}^{elo} and Fig. 1). Due to the interaction of cells this behavior leads to extensional deformations. For the polar model the contractile stress on the single cell level also generates contractile behavior at the collective level. In the nematic model the behavior on the single cell level strongly depends on the shape of the cell. However, the collective behavior shows contractile patterns.

The differences between epithelial and mesenchymal cells, which show extensile and contractile behavior at the collective level, respectively, have been explored in [57]. The different mechanical behavior is associated with strong cell-cell adhesion in epithelial monolayers, which allows for active intercellular force transmission. Weakening this intercellular adhesion results in contractile behavior at the collective level, consistent with the contractile stress on the single cell level. The multiphase field model used in [57] to confirm these findings combines features of our elongation, polar, and nematic

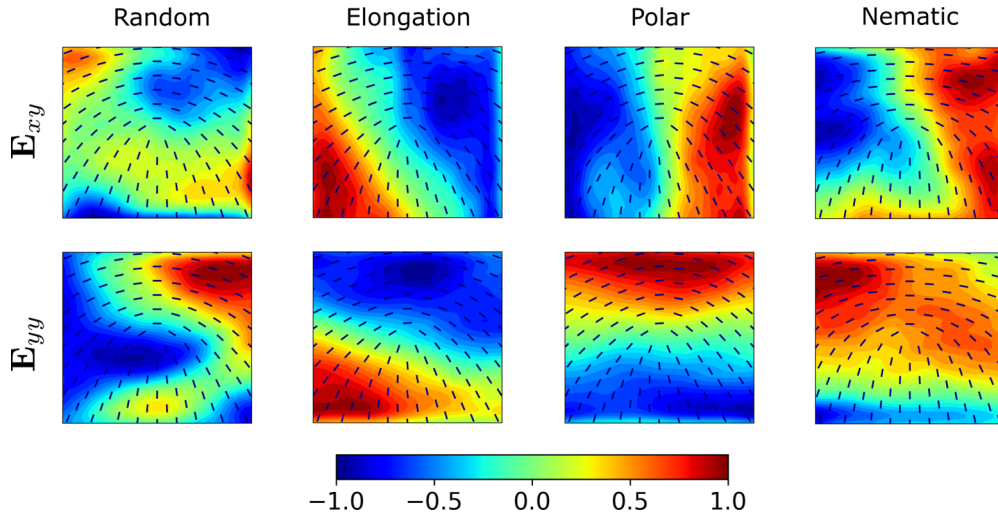


FIG. 8. Average fields for both the xy component (top) and the yy component (bottom) of the strain rate tensor E in the vicinity of $+\frac{1}{2}$ defects for all models: random, elongation, polar, and nematic from left to right. Each plot shows a box of dimension 8×8 centered at the defect core. The average is taken over data of more than 3000 defects for each model.

models. However, the mechanical behavior on the single cell level remains unclear. The purpose of our study is to first fully understand the emerging behavior of each microscopic effect separately, before these effects are combined. In any case the experiments in [57] suggest that additional cell-cell adhesion can change the collective mechanical properties from contractile to extensile in the polar and nematic models. Also in [57] the average velocity in monolayers is compared between extensile and contractile systems at similar density, with larger velocities for the extensile system. Comparing the velocity distribution in Fig. 6 between the elongation model (extensile) and the polar and nematic models (contractile) we find for the average velocity of $+\frac{1}{2}$ defects a consistent behavior (see Table IV). The even higher number for the random model results from the large velocity fluctuations in this model.

C. Active turbulence and vorticity correlation

For large enough activities also flow patterns reminiscent of active turbulence can be found in confluent cell structures. Examples are collectively migrating MDCK cells, fibroblastlike normal rat kidney cells, and HBKCs, which show long-range flows and patterns of vorticity (see, e.g., [7,58]). In models for active liquid crystals such turbulent states emerge as a result of spontaneous defect pair creation. In [12] the velocity field is also analyzed for a multiphase field model. We here follow this approach and compare the four models. Figure 9 shows snapshots of the cell dynamics, visualized using LIC to highlight the active turbulent character of the dynamics. The vorticity is computed from the velocity field as

$\omega = \text{curl } \mathbf{v}$. A vorticity-vorticity correlation function can be computed, which is shown in Fig. 10. It has a well-defined minimum and thus confirms a macroscopic length scale for long-range flows, which is mediated by the activity of the individual cells and their interaction. This length scale more

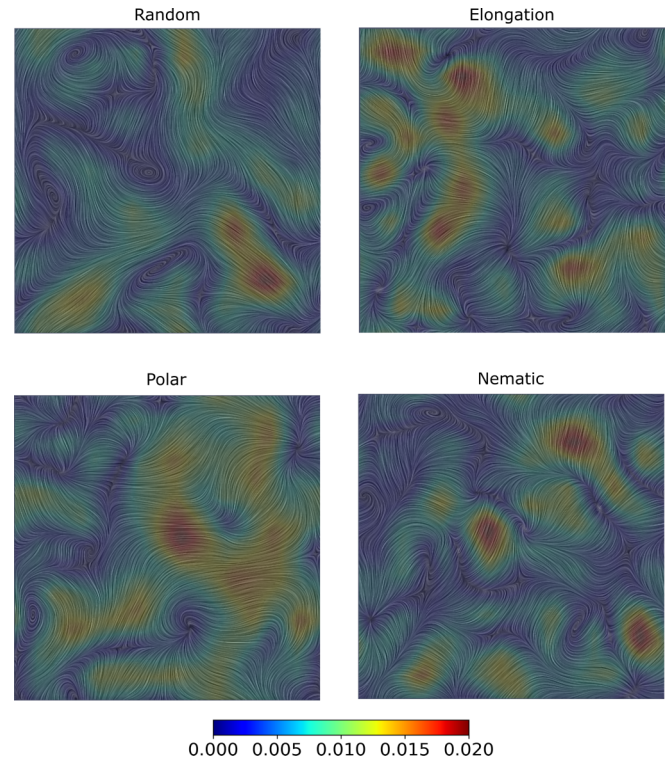


FIG. 9. LIC visualization of cell dynamics for the four models: random, elongation, polar, and nematic (from left to right). Color represents the magnitude of the velocity with the same scaling for all models.

TABLE IV. Average velocities for $+\frac{1}{2}$ defects for all four models.

	Random	Elongation	Polar	Nematic
Velocity	0.954	0.710	0.653	0.294

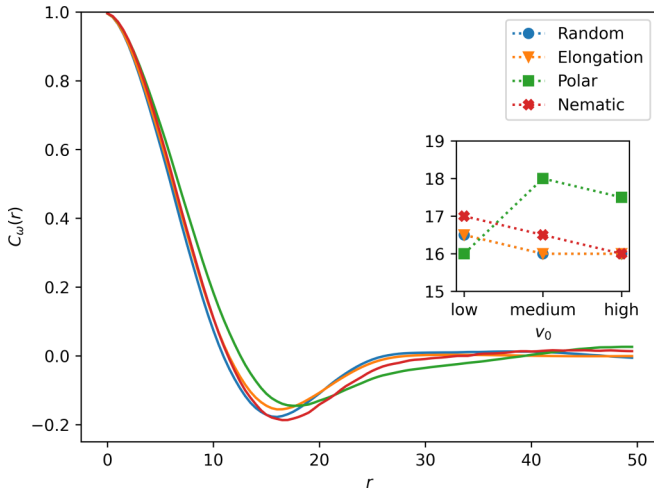


FIG. 10. Vorticity-vorticity correlation function $C_\omega(r) = \langle \omega(r)\omega(0) \rangle / \langle \omega(0)^2 \rangle$ depending on the distance r for all models. The data is averaged over three simulations with the “low” values for the self-propulsion velocity (see Table I). The other values lead to qualitatively similar results. The inset shows the position of the minima for the other activity values.

or less coincides for the four models and only slightly changes with the strength of activity.

As the turbulent collective flow is characterized by the spontaneous emergence of mesoscopic vortices and nematic defects, we also analyze the defect density and creation rate (see Fig. 11). Simulations for active nematics and experiments on MDCK cells (with activity reduced by blebbistatin) [6], show a linear dependency of the defect density on activity. This behavior is qualitatively reproduced by the random, elongation, and polar models. The nematic model shows slight deviations with no consistent slope. The behavior correlates with the defect creation rate. Comparing the absolute values, the nematic model leads to significantly larger defect densities

but lower creation rates, which indicates stronger persistence of defects. In contrast, the random model leads to significantly larger creation rates, which might be explained by the random component of the model.

D. Confinement

While all investigations above consider a large confluent monolayer, we are now concerned with the influence of confinement on the emerging macroscopic behavior. The first multiphase field simulations of such situations consider persistent rotational motion of two cells [10] on adhesive micropatterns. In this model \mathbf{v}_i follows from a reaction-diffusion equation to be solved within each cell. The emerging patterns in concentration of Rho GTPase define a polarity, which determines strength and direction of motion. For a more detailed modeling approach in this direction we refer to [59], and the references therein. Already these simulations, which consider the simplest possible collective motion, show a strong dependency on subcellular features on the emerging behavior. Recent studies with more cells in a rectangular confinement could reproduce sustained oscillation experimentally observed for MDCK cells, human keratinocytes (HaCat), and enterocytes (CaCo2) [60]. The considered multiphase field models in these studies are related to the elongation model [12] and the polar model [40].

To compare the four models we focus on experiments for MDCK cells in circular confinements [61]. They show that confined epithelia exhibit collective low-frequency radial displacement modes and rotational motion, which was partly reproduced in corresponding particle-based simulations [28]. The circular geometry allows one to split the velocity \mathbf{v} into radial and orthoradial components, which can be averaged over all angles to obtain their mean spatial distributions. These values are shown in Fig. 12 for all four models. While the radial component is qualitatively similar in all four models, the orthoradial component qualitatively differs between the

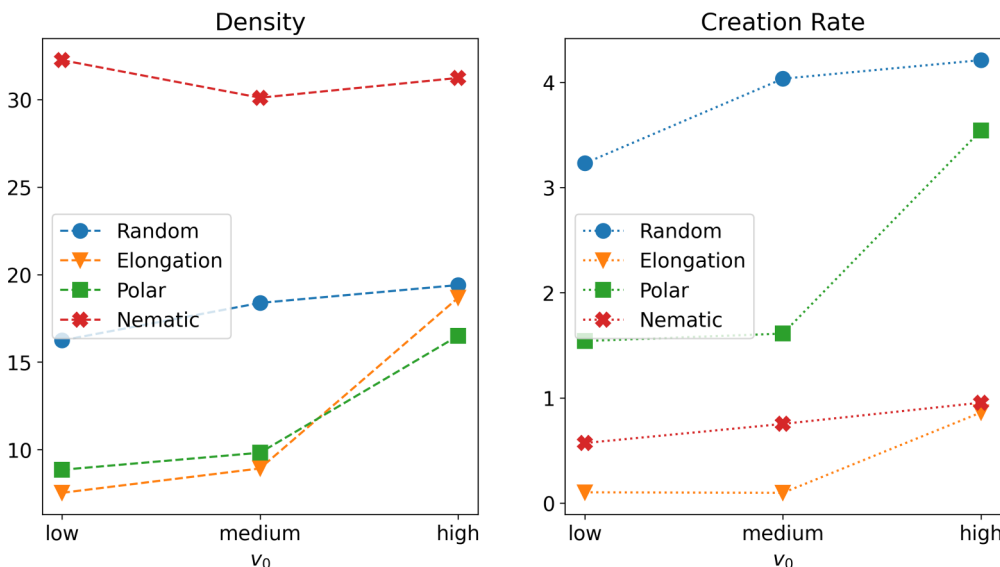


FIG. 11. Averaged defect density (left) and creation rate (right) as a function of activity with low, medium, and high values defined in Table I.

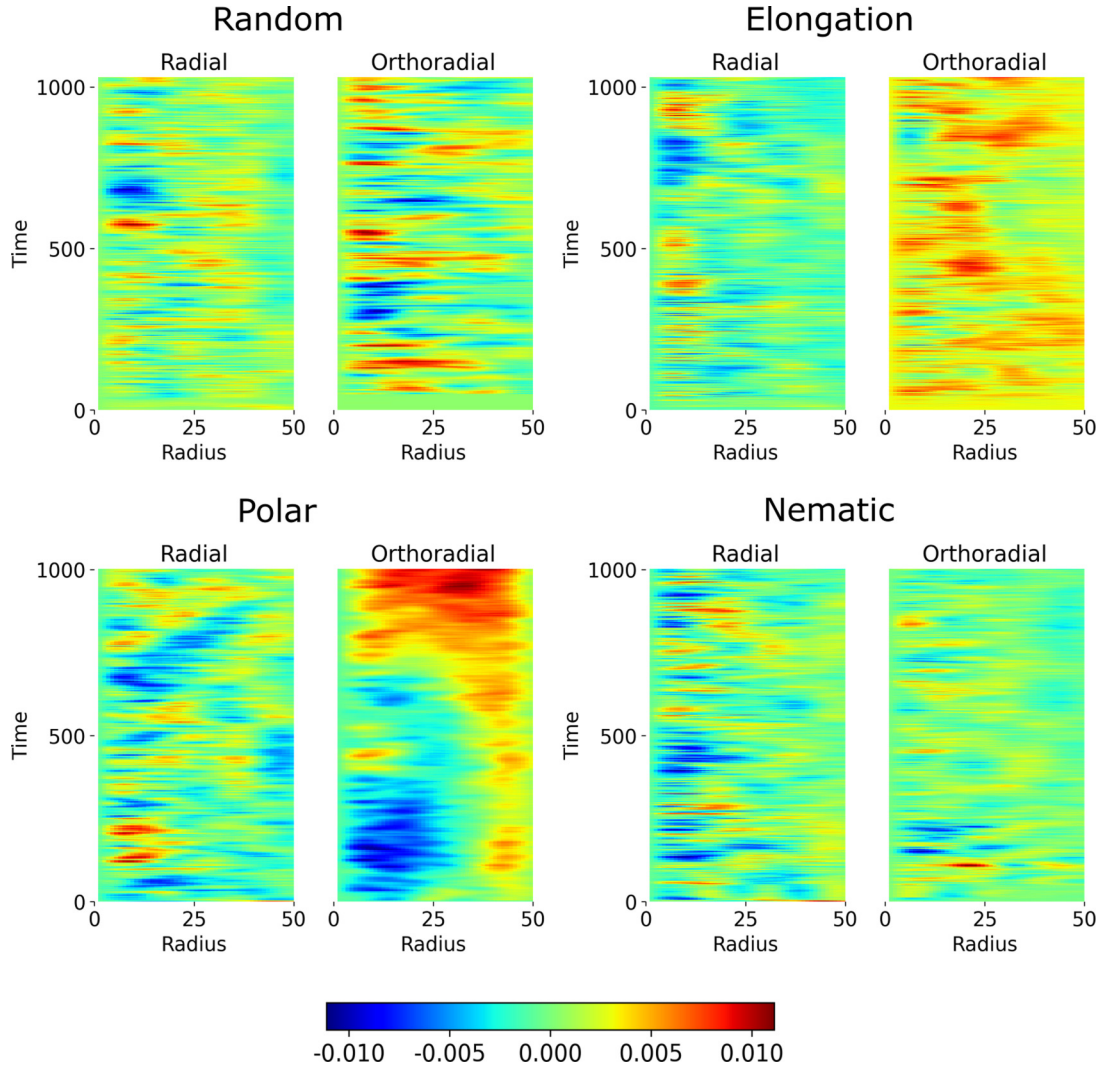


FIG. 12. Kymographs of radial and orthoradial velocity components for the four models: random, elongation, polar, and nematic, from left to right. Corresponding movies of the evolution are provided in the Supplemental Material [62].

models. Only the polar model could reproduce the rotation of the monolayer as a whole and a change in direction of the interior part, which is assumed to be responsible for a comparable size of the confinement and the spatial scale resulting from the vorticity-vorticity correlation in Fig. 10. The simulations are performed with the “medium” values in Table I.

To further analyze the emerging properties in the circular confinement, Fig. 13 shows snapshots of the configuration, highlighting the cell morphology and their neighbor relations. We also compute the bond number $|\Psi_6|$ to be 1 for a perfectly hexagonal arrangement and 0 for an isolated cell (see [14]). The quantity is computed locally and averaged over time, essentially showing a global liquidlike behavior for all four models. The coordination number probability is computed as in Fig. 2, but excluding the cells in contact with the confinement. All four models show a decrease in the mean value as a result of the confinement. The elongation and nematic models also show an increase in the variance if compared with the results in Fig. 2 and thus indicate a shift of the solid-to-liquid transition towards lower activities in the phase diagram.

In real systems confinement has a tremendous effect on the emerging macroscopic behavior and might even induce morphogenesislike processes. Our simulation results indicate that the emerging behavior in confinements strongly depends on subcellular details and the way in which activity is enforced on the cellular level in the modeling approach.

VI. CONCLUSIONS

We use multiphase field models to analyze confluent monolayers of deformable cells. The advantage of such a modeling approach has been pointed out in various recent contributions [9–14]. Cell deformations and detailed cell-cell interactions, as well as subcellular details to resolve the mechanochemical interactions underlying cell migration can naturally be handled. Also topological changes, such as rosettes or $T1$ transitions, follow naturally in a multiphase field framework. Using efficient numerics and appropriate computing power we analyze the emerging macroscopic behavior in such models and compare with known universal features of cell

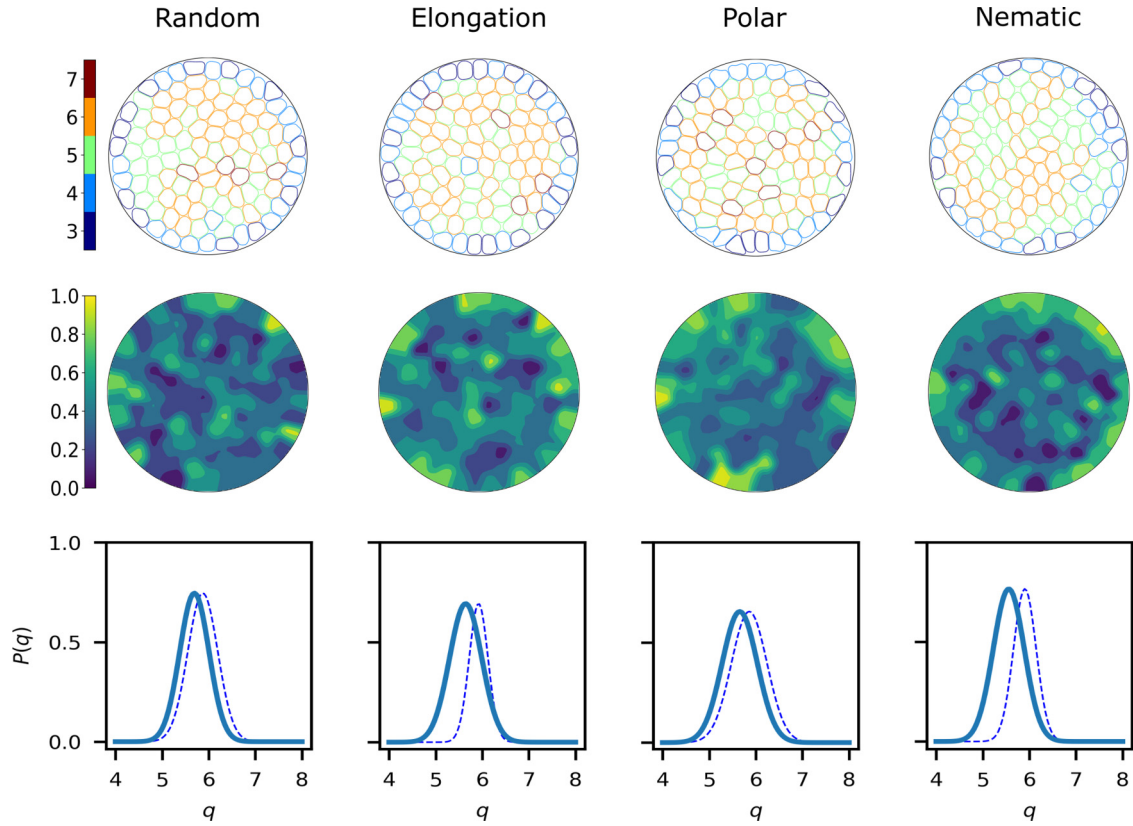


FIG. 13. First row: Cell morphology and number of neighbors. Second row: Time-averaged bond number. Third row: Coordination number probability computed excluding cells in contact with confinement. The corresponding curves from Fig. 2 are shown for comparison (dashed curves).

monolayers and epithelia tissue. We consider four different minimal models. They all follow the same methodology and only differ at microscopic details on the incorporation of activity: The random model [14] determines the direction of motion on the single cell level by a stochastic process, and the elongation model [12] aligns the direction of motion with the long axis of the cell and two models, the polar [13] and a nematic model, which use subcellular details to determine strength and direction of motion on a single cell level.

Various of the known generic features of confluent monolayers are reproduced by all four models, highlighting the robustness of these features on microscopic details. This includes coordination number distribution, which leads after appropriate calibration of parameters to similar phase diagrams as obtained with vertex and Voronoi models [19]. Other common features are the spontaneous formation of vortices and topological defects as well as the emergence of active turbulent flows.

TABLE V. Comparison of considered emerging properties. ✓ indicates observed agreement, X indicates disagreement, and (✓) indicates only qualitative agreement with universal feature. If experimental data are not available or insufficient for a comparison, only similarities or differences of the models are noted. This summary only accounts for the specific form of the models and the considered parameters in this paper; for more details see the sections above.

	Random	Elongation	Polar	Nematic
Coordination number distribution	(✓)	(✓)	(✓)	(✓)
Shape variability	(✓)	✓	✓	(✓)
Rosette ratio		Differences between models		
Velocity distribution of topological defects		Differences between models		
Correlation between direction of motion and orientation of defect	X	✓	✓	(✓)
Elastic property of $+\frac{1}{2}$ defect	X	Extensile	Contractile	Contractile
Active turbulence	(✓)	(✓)	(✓)	(✓)
Vorticity-vorticity correlation		Similar for all models		
Dependency of defect density on activity	Linear	Linear	Linear	Constant
Rotational motion in circular confinement	X	(✓)	X	X

However, the four models also lead to different results if more quantitative measures are considered. This becomes apparent for the deformation of cells. While the shape variability of the cells can be described by a k -gamma distribution over a broad range of parameters for all four models, the narrow range of the parameter k found in [5] for various epithelia systems, could only be reproduced by the elongation and polar model. Not only geometrical properties of the cells, but also topological features differ between the four models. The ratio of multicellular rosettes depends on the microscopic details. As these rosettes provide an efficient mechanism for tissue remodeling (see, e.g., [49]), these differences need to be considered in further model extensions. The most striking differences between the four models are found by analyzing the emerging nematic liquid crystal properties of the monolayer and its topological defects. The different role of $+\frac{1}{2}$ and $-\frac{1}{2}$ defects in active nematodynamics can only be reproduced by the elongation, polar, and nematic models. However, the mechanical properties differ. The elongation model is constructed to produce extensile behavior on the multicellular level. In the polar model the contractile behavior on the single cell level carries over to the multicellular level and also the nematic model, where the properties on the single cell level depend on shape, leads to contractile behavior on the multicellular level. As suggested by the experiments on MDCK cells [57], the emerging mechanical properties of these models on the multicellular level might be influenced by changing the considered cell-cell interactions. Also the simulations in

confinement bring differences of the models to light. Induced global rotation, as observed in circular confinements for MDCK cells in [61] and reproduced by particle-based simulations [28] could only be observed with the polar model. However, all models show a slight change in coordination number distribution if considered in confinements. A summary of these comparisons is given in Table V.

The comprehensive comparison of multiphase field models for confluent cell monolayers shows the strong effect of the way activity is considered on a single cell level and highlights the need to take these effects into account for predictive simulation results at the multicellular level. However, the results also show the robustness of these models in producing generic qualitative features for cell monolayers and epithelia tissue. The flexibility of multiphase field models, not only in terms of cell deformability and topological changes, such as formation of rosettes and $T1$ transitions, but also in incorporating mechanochemical effects on a single cell level and for cell-cell interactions offers this modeling approach a huge potential for multiscale simulations of multicellular dynamics.

ACKNOWLEDGMENTS

A.V. acknowledges support by the German Research Foundation (DFG) under Grant No. FOR3013. We further acknowledge computing resources provided at Jülich Supercomputing Center under Grant No. pfamdis and at ZIH at TU Dresden.

-
- [1] P. Friedl and D. Gilmour, Collective cell migration in morphogenesis, regeneration and cancer, *Nat. Rev. Mol. Cell Biol.* **10**, 445 (2009).
 - [2] P. Rorth, Collective cell migration, *Annu. Rev. Cell Dev. Biol.* **25**, 407 (2009).
 - [3] E. Scarpa and R. Mayor, Collective cell migration in development, *J. Cell Biol.* **212**, 143 (2016).
 - [4] C. Malinverno, S. Corallino, F. Giavazzi, M. Bergert, Q. Li, M. Leoni, A. Disanza, E. Frittoli, A. Oldani, E. Martini *et al.*, Endocytic reawakening of motility in jammed epithelia, *Nat. Mater.* **16**, 587 (2017).
 - [5] L. Atia, D. Bi, Y. Sharma, J. A. Mitchel, B. Gweon, S. A. Koehler, S. J. DeCamp, B. Lan, J. H. Kim, R. Hirsch *et al.*, Geometric constraints during epithelial jamming, *Nat. Phys.* **14**, 613 (2018).
 - [6] T. B. Saw, A. Doostmohammadi, V. Nier, L. Kocgozlu, S. Thampi, Y. Toyama, P. Marcq, C. T. Lim, J. M. Yeomans, and B. Ladoux, Topological defects in epithelia govern cell death and extrusion, *Nature (London)* **544**, 212 (2017).
 - [7] C. Blanch-Mercader, V. Yashunsky, S. Garcia, G. Duclos, L. Giomi, and P. Silberzan, Turbulent Dynamics of Epithelial Cell Cultures, *Phys. Rev. Lett.* **120**, 208101 (2018).
 - [8] F. Graner and J. A. Glazier, Simulation of Biological Cell Sorting Using a Two-Dimensional Extended Potts-Model, *Phys. Rev. Lett.* **69**, 2013 (1992).
 - [9] M. Nonomura, Study on multicellular systems using a phase field model, *PLoS One* **7**, e33501 (2012).
 - [10] B. A. Camley, Y. Zhang, Y. Zhao, B. Li, E. Ben-Jacob, H. Levine, and W.-J. Rappel, Polarity mechanisms such as contact inhibition of locomotion regulate persistent rotational motion of mammalian cells on micropatterns, *Proc. Nat. Acad. Sci. USA* **111**, 14770 (2014).
 - [11] B. Palmieri, Y. Bresler, D. Wirtz, and M. Grant, Multiple scale model for cell migration in monolayers: Elastic mismatch between cells enhances motility, *Sci. Rep.* **5**, 11745 (2015).
 - [12] R. Mueller, J. M. Yeomans, and A. Doostmohammadi, Emergence of Active Nematic Behavior in Monolayers of Isotropic Cells, *Phys. Rev. Lett.* **122**, 048004 (2019).
 - [13] D. Wenzel, S. Praetorius, and A. Voigt, Topological and geometrical quantities in active cellular structures, *J. Chem. Phys.* **150**, 164108 (2019).
 - [14] B. Loewe, M. Chiang, D. Marenduzzo, and M. C. Marchetti, Solid-Liquid Transition of Deformable and Overlapping Active Particles, *Phys. Rev. Lett.* **125**, 038003 (2020).
 - [15] T. Nagai and H. Honda, A dynamic cell model for the formation of epithelial tissues, *Philos. Mag. B* **81**, 699 (2001).
 - [16] D. B. Staple, R. Farhadifar, J.-C. Roeper, B. Aigouy, S. Eaton, and F. Juelicher, Mechanics and remodelling of cell packings in epithelia, *Eur. Phys. J. E* **33**, 117 (2010).
 - [17] A. G. Fletcher, M. Osterfield, R. E. Baker, and S. Y. Shvartsman, Vertex models of epithelial morphogenesis, *Biophys. J.* **106**, 2291 (2014).
 - [18] B. Li and S. X. Sun, Coherent motions in confluent cell monolayer sheets, *Biophys. J.* **107**, 1532 (2014).

- [19] D. Bi, X. Yang, M. C. Marchetti, and M. L. Manning, Motility-Driven Glass and Jamming Transitions in Biological Tissues, *Phys. Rev. X* **6**, 021011 (2016).
- [20] G. S. Redner, A. Baskaran, and M. F. Hagan, Reentrant phase behavior in active colloids with attraction, *Phys. Rev. E* **88**, 012305 (2013).
- [21] R. M. Navarro and S. M. Fielding, Clustering and phase behaviour of attractive active particles with hydrodynamics, *Soft Matter* **11**, 7525 (2015).
- [22] S. Aland, H. Hatzikirou, J. Lowengrub, and A. Voigt, A mechanistic collective cell model for epithelial colony growth and contact inhibition, *Biophys. J.* **109**, 1347 (2015).
- [23] V. Prymidis, S. Paliwal, M. Dijkstra, and L. Fillion, Vapour-liquid coexistence of an active Lennard-Jones fluid, *J. Chem. Phys.* **145**, 124904 (2016).
- [24] F. Alaïmo, S. Praetorius, and A. Voigt, A microscopic field theoretical approach for active systems, *New J. Phys.* **18**, 083008 (2016).
- [25] G. Duclos, C. Blanch-Mercader, V. Yashunsky, G. Salbreux, J. F. Joanny, J. Prost, and P. Silberzan, Spontaneous shear flow in confined cellular nematics, *Nat. Phys.* **14**, 728 (2018).
- [26] D. Dell'Arciprete, M. L. Blow, A. T. Brown, F. D. C. Farrell, J. S. Lintuvuori, A. F. McVey, D. Marenduzzo, and W. C. K. Poon, A growing bacterial colony in two dimensions as an active nematic, *Nat. Commun.* **9**, 4190 (2018).
- [27] A. Doostmohammadi, J. Ignes-Mullol, J. M. Yeomans, and F. Sagues, Active nematics, *Nat. Commun.* **9**, 3246 (2018).
- [28] V. Hakim and P. Silberzan, Collective cell migration: A physics perspective, *Rep. Prog. Phys.* **80**, 076601 (2017).
- [29] R. Alert and X. Trepat, Physical models of collective cell migration, *Annu. Rev. Condens. Matter Phys.* **11**, 77 (2020).
- [30] A. Moure and H. Gomez, Phase-field modeling of individual and collective cell migration, *Arch. Comput. Meth. Eng.* **28**, 311 (2021).
- [31] W. Marth, S. Praetorius, and A. Voigt, A mechanism for cell motility by active polar gels, *J. R. Soc., Interface* **12**, 20150161 (2015).
- [32] W. Marth and A. Voigt, Collective migration under hydrodynamic interactions: A computational approach, *Interface Focus* **6**, 20160037 (2016).
- [33] W. Marth, S. Aland, and A. Voigt, Margination of white blood cells: A computational approach by a hydrodynamic phase field model, *J. Fluid Mech.* **790**, 389 (2016).
- [34] Y. Fily and M. C. Marchetti, Athermal Phase Separation of Self-Propelled Particles with No Alignment, *Phys. Rev. Lett.* **108**, 235702 (2012).
- [35] A. Wysocki, R. G. Winkler, and G. Gompper, Cooperative motion of active Brownian spheres in three-dimensional dense suspensions, *Europhys. Lett.* **105**, 48004 (2014).
- [36] E. Tjhung, D. Marenduzzo, and M. E. Cates, Spontaneous symmetry breaking in active droplets provides a generic route to motility, *Proc. Natl. Acad. Sci. USA* **109**, 12381 (2012).
- [37] F. Ziebert, S. Swaminathan, and I. S. Aranson, Model for self-polarization and motility of keratocyte fragments, *J. R. Soc. Interface* **9**, 1084 (2012).
- [38] C. A. Whitfield, D. Marenduzzo, R. Voituriez, and R. J. Hawkins, Active polar fluid flow in finite droplets, *Eur. Phys. J. E* **37**, 8 (2014).
- [39] J. Loeber, F. Ziebert, and I. S. Aranson, Collisions of deformable cells lead to collective migration, *Sci. Rep.* **5**, 9172 (2015).
- [40] D. Wenzel, M. Nestler, S. Reuther, M. Simon, and A. Voigt, Defects in active nematics—Algorithms for identification and tracking, *Comput. Meth. Appl. Math.* **21**, 683 (2021).
- [41] Luca Giomi and Antonio DeSimone, Spontaneous Division and Motility in Active Nematic Droplets, *Phys. Rev. Lett.* **112**, 147802 (2014).
- [42] T. Gao and Z. Li, Self-Driven Droplet Powered by Active Nematics, *Phys. Rev. Lett.* **119**, 108002 (2017).
- [43] S. Vey and A. Voigt, AMDiS: Adaptive multidimensional simulations, *Comput. Vis. Sci.* **10**, 57 (2007).
- [44] T. Witkowski, S. Ling, S. Praetorius, and A. Voigt, Software concepts and numerical algorithms for a scalable adaptive parallel finite element method, *Adv. Comput. Math.* **41**, 1145 (2015).
- [45] S. Praetorius and A. Voigt, Collective cell behavior—A cell-based parallelization approach for a phase field active polar gel model, in *NIC Symposium 2018*, edited by K. Binder, M. Müller, and A. Trautmann (Forschungszentrum Jülich GmbH, Jülich, 2018), pp. 369–376.
- [46] J. T. Blankenship, S. T. Backovic, J. S. P. Sanny, O. Weitz, and J. A. Zallen, Multicellular rosette formation links planar cell polarity to tissue morphogenesis, *Dev. Cell* **11**, 459 (2006).
- [47] M. J. Harding, H. F. McGraw, and A. Nechiporuk, The roles and regulation of multicellular rosette structures during morphogenesis, *Development* **141**, 2549 (2014).
- [48] D. Hava, U. Forster, M. Matsuda, S. Cui, B. A. Link, J. Eichhorst, B. Wiesner, A. Chitnis, and S. Abdelilah-Seyfried, Apical membrane maturation and cellular rosette formation during morphogenesis of the zebrafish lateral line, *J. Cell Sci.* **122**, 687 (2009).
- [49] L. Yan and D. Bi, Multicellular Rosettes Drive Fluid-Solid Transition in Epithelial Tissues, *Phys. Rev. X* **9**, 011029 (2019).
- [50] I. F. Sbalzarini and P. Koumoutsakos, Feature point tracking and trajectory analysis for video imaging in cell biology, *J. Struct. Biol.* **151**, 182 (2005).
- [51] J. Schindelin *et al.*, Fiji: An open-source platform for biological-image analysis, *Nat. Methods* **9**, 676 (2012).
- [52] S. J. DeCamp, G. S. Redner, A. Baskaran, M. F. Hagan, and Z. Dogic, Orientational order of motile defects in active nematics, *Nat. Mater.* **14**, 1110 (2015).
- [53] A. U. Oza and J. Dunkel, Antipolar ordering of topological defects in active liquid crystals, *New J. Phys.* **18**, 093006 (2016).
- [54] L. Giomi, M. J. Bowick, P. Mishra, R. Sknepnek, and M. C. Marchetti, Defect dynamics in active nematics, *Philos. Trans. R. Soc. London, Ser. A* **372**, 20130365 (2014).
- [55] K. Kawaguchi, R. Kageyama, and M. Sano, Topological defects control collective dynamics in neural progenitor cell cultures, *Nature (London)* **545**, 327 (2017).
- [56] G. Duclos, C. Erlenkämper, J.-P. Joanny, and P. Silberzan, Topological defects in confined populations of spindle-shaped cells, *Nat. Phys.* **13**, 58 (2017).

- [57] L. Balasubramaniam, A. Doostmohammadi, T. B. Saw, G. H. N. S. Narayana, R. Mueller, T. Dang, M. Thomas, S. Gupta, S. Sonam, A. S. Yap *et al.*, Investigating the nature of active forces in tissues reveals how contractile cells can form extensile monolayers, *Nat. Mater.* **20**, 1156 (2021).
- [58] L. Petitjean, M. Reffay, E. Grasland-Mongrain, M. Poujade, B. Ladoux, A. Buguin, and P. Silberzan, Velocity fields in a collectively migrating epithelium, *Biophys. J.* **98**, 1790 (2010).
- [59] W. Marth and A. Voigt, Signaling networks and cell motility: A computational approach using a phase field description, *J. Math. Biol.* **69**, 91 (2014).
- [60] G. Peyret, R. Mueller, J. d'Alessandro, S. Begnaud, P. Marcq, R.-M. Mege, J. M. Yeomans, A. Doostmohammadi, and B. Ladoux, Sustained oscillations of epithelial cell sheets, *Biophys. J.* **117**, 464 (2019).
- [61] M. Deforet, V. Hakim, H. G. Yevick, G. Duclos, and P. Silberzan, Emergence of collective modes and tri-dimensional structures from epithelial confinement, *Nat. Commun.* **5**, 3747 (2014).
- [62] See Supplemental Material at <http://link.aps.org/supplemental/10.1103/PhysRevE.104.054410> for corresponding movies to kymographs in Fig. 12 showing the evolution of the cells in the circular confinement for the four different models. The cells are visualized by the zero-level line of the phase field variables ϕ_i .